

## Article

# Effects of Water–Rock Interaction on the Permeability of the Near-Well Reservoir in an Enhanced Geothermal System

Bo Feng <sup>1</sup>, Zhenpeng Cui <sup>1</sup>, Xiyao Liu <sup>1</sup>, Shuantong Shangguan <sup>2</sup>, Xiaofei Qi <sup>2</sup> and Shengtao Li <sup>3,\*</sup><sup>1</sup> College of Environment and Resources, Jilin University, Changchun 130021, China<sup>2</sup> No. 2 Exploration Team Hebei Bureau of Coal Geological Exploration, Xingtai 054000, China<sup>3</sup> Center for Hydrogeology and Environmental Geology Survey, China Geological Survey, Baoding 071051, China

\* Correspondence: li.st@163.com

**Abstract:** During the operation of an enhanced geothermal system (EGS), the non-equilibrium temperature, pressure, and hydrochemistry caused by fluid injection intensify water–rock interactions, induce the mineral dissolution and precipitation in the reservoir near an injection well (also referred to as the near-well reservoir), and change reservoir permeability, thus affecting continuous and efficient geothermal exploitation. Based on the investigation of the M-1 injection well of the EGS in the Matouying uplift of Hebei Province, China, a THC reactive solute transport model using the TOUGHREACT program was established in this study to explore the mineral dissolution and precipitation laws of the near-well reservoir and their influencing mechanisms on the reservoir porosity and permeability in the long-term fluid injection of this well. As indicated by the results, the dissolution of primary feldspar and chlorite and the precipitation of secondary minerals (mainly dolomite and illite) occurred and water–rock interaction significantly reduced the porosity and permeability of the near-well reservoir in the long-term continuous injection process. Appropriate reduction in the injection flow rate, injection temperature, and the Mg<sup>2+</sup> and K<sup>+</sup> contents in the injected water can help inhibit the formation of secondary minerals and delay the plugging process of the near-well reservoir.

**Keywords:** enhanced geothermal system; water–rock interaction; secondary precipitation; reactive solute transport; TOUGHREACT



**Citation:** Feng, B.; Cui, Z.; Liu, X.; Shangguan, S.; Qi, X.; Li, S. Effects of Water–Rock Interaction on the Permeability of the Near-Well Reservoir in an Enhanced Geothermal System. *Energies* **2022**, *15*, 8820. <https://doi.org/10.3390/en15238820>

Academic Editor: Dameng Liu

Received: 31 October 2022

Accepted: 21 November 2022

Published: 23 November 2022

**Publisher's Note:** MDPI stays neutral with regard to jurisdictional claims in published maps and institutional affiliations.



**Copyright:** © 2022 by the authors. Licensee MDPI, Basel, Switzerland. This article is an open access article distributed under the terms and conditions of the Creative Commons Attribution (CC BY) license (<https://creativecommons.org/licenses/by/4.0/>).

## 1. Introduction

The high dependence on fossil fuels in today's society not only leads to a global energy crisis but also further aggravates challenges such as greenhouse gas emissions and environmental pollution [1,2]. The use of new clean energy will help solve these problems [3,4]. Compared with traditional energy sources and other renewable energy sources, geothermal energy has many engineering and environmental advantages, such as non-seasonal dependence and a small area for resource extraction, and is thus an ideal new clean energy [5,6]. It can be used for many purposes, such as heating and power generation [7]. At the current energy consumption rate, it is estimated that the global energy demand in 2800 can be met as long as 1% of the geothermal resources in the crust are fully exploited and utilized [8,9].

An EGS refers to an artificial geothermal system in which geothermal energy is economically extracted from low-permeability rock masses by artificially creating geothermal reservoirs [10]. During geothermal exploitation using an EGS, circulating fluids (usually water) are injected through injection wells to make them move along the fracture network and exchange heat with surrounding rocks, and then high-temperature fluids can be extracted from production wells for power generation and comprehensive utilization [11]. This process involves sufficient contact between the low-temperature injected fluids and the

high-temperature rock masses in deep reservoirs. However, relevant studies have shown that the changes in temperature, pressure, and hydrochemistry caused by the heat transfer fluids lead to a sustained non-equilibrium between solids and solutes and further drive fluid–rock interactions, leading to different degrees of mineral dissolution and precipitation which change the permeability of the near-well reservoir and affect sustainable and efficient geothermal exploitation [12].

Because of the difficulty, long period, and high costs of actual operation and monitoring, numerical simulation technology is considered an effective means to conduct site-scale analysis and prediction. In recent years, researchers in related fields have carried out massive laboratory experiments and numerical simulations to explore the dissolution and precipitation of minerals induced by the interactions between circulating fluids and geothermal reservoir rocks and the resultant changes in geothermal reservoir permeability during the production and operation of an open-loop geothermal system. Borgia et al. analyzed the feasibility of using CO<sub>2</sub> as the transfer fluids of an EGS through numerical simulations, and the results showed that the injection of CO<sub>2</sub> mixed with water inhibited secondary precipitation and effectively prolonged the operating life of the EGS but limited the heat extraction rate [12]. Driba et al. established a one-dimensional THC reactive solute transport model based on Phreeqc and OpenGeosys to explore the effects of the chemical composition of injected fluids on the deep geothermal reservoir permeability during the reinjection of low-temperature brine [13]. Ren et al. proposed a mixed discretization method based on embedded meshes and accurately and effectively determined the coupling process of multiphase flow and geomechanics in fractured reservoirs [14]. Salimzadeh et al. established a 3D multifield coupling model for fractured geothermal reservoirs and explored the influence of low-temperature fluid injection on fracture channel deformation [15]. Pei et al. established a new flow and geomechanical coupling model and effectively captured the fracture deformation process in unconventional fractured reservoirs [16]. Li et al. improved the calculation efficiency while maintaining relatively high accuracy by combining the embedded discrete fracture model (EDFM) and the extended finite element method (XFEM) [17]. These studies provide references and bases for further improving and expanding the reactive solute transport model [18].

Regenspurg et al. carried out a hydrogeochemistry equilibrium calculation based on the collection, testing, and analysis of numerous samples to explore the cause and mechanism of the severe plugging of production wells at the site in Groß Schönebeck, Germany, revealing that frequent well shutdown constantly made the metal-rich fluids oversaturated in the process of reacting with the wellbore and cooling, thus exacerbating the plugging of geothermal wells [19]. Based on a large number of experimental studies, as well as reinjection experiments and hydrogeochemical simulations, Ma et al. proved that chemical plugging caused by carbonate and silicate was the main reason for the significant decrease in the injection flow rate of Well Xianyang 2 over time [20]. Yanaze et al. established a geochemical plugging model for the Sumikawa Geothermal Power Plant to predict the decrease in permeability caused by the deposition of silica scale on the site and found that reducing the silica concentration and the injection flow rate can effectively delay the decrease in the reservoir permeability [21]. Zhao et al. carried out high-temperature and high-pressure static experiments and hydrogeochemical simulations based on the PHREEQC program to determine the interactions between different injected water bodies and high-temperature granites, finding that using low-salinity water as the injected water could reduce the possibility of geothermal reservoir plugging [22]. Ke et al. used similar methods to evaluate the effect of different fluids on the release of typical minerals in the FORGE site [23].

The secondary precipitation caused by fluid injection has been analyzed in the above studies. However, most of these studies employed small-scale static simulations and experiments, which cannot reflect the dynamic process occurring in actual reservoirs. Moreover, there is still a lack of targeted research on the effects of dynamic near-well water–rock interactions and solute transport on reservoir permeability during long-term

injection. Based on the investigation of injection well M-1 in the EGS in the Matouying uplift of Hebei Province, China, this study established a THC reactive solute transport model using the TOUGHREACT program and analyzed and predicted the laws of the mineral dissolution and precipitation caused by water-rock reactions and solute transport and their influence on the near-well reservoir permeability in the long-term injection of this well. This study provides a technical reference and theoretical basis for the long-term stable operation of geothermal systems.

## 2. Geological Conditions of Regional Geothermal Resources

The study area is located in the Matouying uplift of Leting County, Tangshan City, eastern Hebei Province [24]. The Matouying uplift is a significant positive secondary tectonic unit within the Huanghua depression in North China. It is bounded by the Mabei fault and connected to the Leting sag in the north, bounded by the Boge Zhuang fault and connected to the Nanpu sag in the west, and is bounded by the Hongfangfang fault and adjacent to the Shijiutuo sag in the south (Figure 1). The tectonic pattern consisting of the high uplift and deep sags creates favorable geological conditions for the upward migration of deep heat flow and the convergence of lateral heat flow toward the uplift area [25]. The Matouying uplift has terrestrial heat flow of greater than 75 mW/m<sup>2</sup>, which is higher than the global average, making this uplift a favorable prospect area for the exploitation of deep geothermal resources in Hebei Province [26].

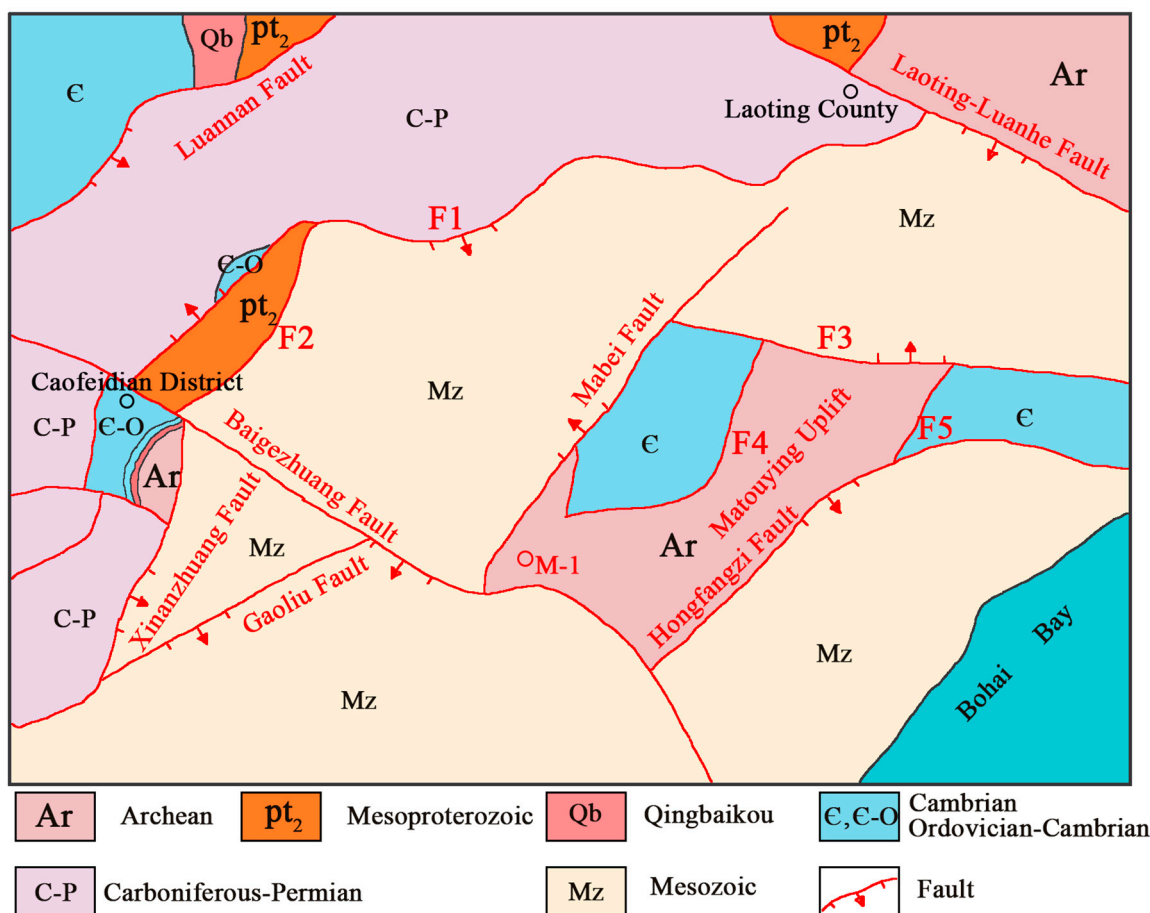


Figure 1. Tectonic location of the study area.

The EGS project in the Matouying uplift is located in southern Dazhuanghe Village, Caofeidian District, Tangshan City. This project consists of injection well M-1 and production well M-2, which are about 200 m apart. Well M-1 has a final hole depth of 4502.11 m, with the water filtering interval at a depth of 4188.08–4502.11 m. This well has a water

temperature of up to 150 °C at a depth of 3960 m. The main strata encountered during the drilling of this well include the Quaternary (Q), the Neogene Minghuazhen ( $N_{2m}$ ) and Guantao formations ( $N_{1g}$ ), and the Archean Baimiao Formation ( $Arb$ ). The Cenozoic strata in the upper part of this well mainly include clay, sandstones, and mudstones, while the Archean Baimiao Formation in the lower part is mainly composed of metamorphic granodiorites, metamorphic tonalites, metamorphic hornblende monzogranites, and biotite plagiogneisses, indicating apparent migmatization [27].

### 3. Numerical Simulation Method

#### 3.1. Simulator

The simulator used in this study was the TOUGHREACT program developed by the Lawrence Berkeley National Laboratory. By introducing the reactive solute transport process into the basic framework of the simulator TOUGH2 for non-isothermal flows of multicomponent and multiphase fluids, this simulator couples the flow, heat transfer, solute transport, and geochemical reaction processes of underground multiphase fluids while considering the thermophysicochemical processes under conditions of different temperatures, pressure, water saturation, and ionic strength [28]. TOUGHREACT is suitable for one-, two-, and three-dimensional porous and fractured media with physical and chemical heterogeneity, as well as any number of gas-, liquid-, and solid-phase chemicals. Therefore, this program is widely applied to the exploitation and utilization of geothermal energy, the geological storage of carbon dioxide, pollutant migration and remediation, and nuclear waste disposal [29].

#### 3.2. Governing Equations

The main governing equations used by TOUGHREACT are introduced as follows. For numerical simulations, the mass and energy conservation equation is the most basic and core equation, and its generalized expression is shown in Equation (1).

$$\frac{d}{dt} \int_{V_n} M^K dV = \int_{\Gamma_n} F^K \cdot n d\Gamma + \int_{V_n} q^K dV \quad (1)$$

where  $t[s]$  is the time;  $n$  is the current grid;  $\kappa$  is the different components;  $\Gamma_n [m^2]$  is the grid connection area;  $V_n [m^3]$  is the grid volume;  $M^K$ ,  $F^K$ , and  $q^K$  are the cumulative item, migration (i.e., inflow or outflow) item, and source-sink item of mass or energy, respectively.

Chemical transport equations (derived from mass conservation) have the same structure as fluid and heat flow equations, and the equation of multicomponent chemical transport in the liquid phase is expressed as Equation (2).

$$\begin{aligned} \frac{\Delta t}{V_n} \sum_m A_{nm} \left[ u_{nm}^{k+1} C_{nm}^{(j), k=1, s+\frac{1}{2}} + D_{nm} \frac{C_m^{(j), k=1, s+\frac{1}{2}} - C_n^{(j+1), k=1, s+\frac{1}{2}}}{d_{nm}} \right] \\ = \Delta M_n^{(j), k+1} - q_n^{(j), k+1} \Delta t - R_n^{(j), k+1, s} \Delta t \quad J = 1, 2, \dots, N_c \end{aligned} \quad (2)$$

The transport of aqueous and gaseous species through advection and molecular diffusion are considered for both liquid and gas phases in this simulator. Acid-base and redox are considered under the local equilibrium assumption. Depending on the computer memory and CPU performance, any number of chemical species in the liquid, gas, and solid phases can be accommodated. The dissolution and precipitation processes of minerals are characterized by two mechanisms, i.e., thermodynamic equilibrium and reaction kinetic equilibrium. The thermodynamic governing equations used by TOUREACT are shown in Equations (3) and (4), and the governing equations of reaction kinetics based on the transition state theory are shown in Equations (5) and (6).

$$SI_m = \log_{10} \Omega_m = 0 \quad (3)$$

$$\Omega_m = K_m^{-1} \prod_{j=1}^{Nc} c_j^{v_{mj}} \gamma_j^{v_{mj}} \quad m = 1, \dots, Np \quad (4)$$

$$r = A_m k_m \left[ 1 - \left( \frac{Q}{K} \right)^\mu \right]^n \quad (5)$$

$$k = k_{25}^{nu} \exp \left[ \frac{-E_a^{nu}}{R} \left( \frac{1}{T} - \frac{1}{298.15} \right) \right] + k_{25}^H \exp \left[ \frac{-E_a^H}{R} \left( \frac{1}{T} - \frac{1}{298.15} \right) \right] \alpha_H^{n_H} + k_{25}^{OH} \exp \left[ \frac{-E_a^{OH}}{R} \left( \frac{1}{T} - \frac{1}{298.15} \right) \right] \alpha_{OH}^{n_{OH}} \quad (6)$$

where  $m$  is the mineral serial number;  $SI$  is the saturation index of minerals;  $\Omega$  is the saturation of minerals;  $K$  is the thermodynamic equilibrium constant;  $\gamma$  is the activity coefficient;  $r$  [mol/s] is the mineral reaction rate (it is positive for dissolution and negative for precipitation);  $A$  [g/cm<sup>2</sup>] is the reaction specific surface area of minerals;  $k$  [mol/(L·s)] is the reaction rate constant related to temperature;  $Q$  is the reaction quotient;  $\mu$  and  $n$  are laboratory empirical parameters;  $k_{25}$  [mol/(L·s)] is the reaction rate constant at 25 °C;  $E_a$  [KJ/mol] is the activation energy;  $R$  [J/mol/K] is the gas constant;  $T$  [K] is the absolute temperature, and  $\alpha$  [mol/L] is the activity.

The dissolution and precipitation of minerals lead to changes in porosity and permeability, which further affect the fluid flow and solute transport process. Therefore, it is necessary to accurately describe the dynamic changes in porosity and permeability. When the numerical simulations of water-rock reactions are performed using TOUGHREACT, the medium porosity is determined using Equation (7).

$$\varphi = 1 - \sum_{m=1}^{nm} fr_m - fr_u \quad (7)$$

where  $\varphi$  is porosity;  $nm$  is the number of mineral species;  $fr_m$  is the volume fraction of mineral  $m$ ; and  $fr_u$  is the volume fraction of unreactive rock.

As  $fr_m$  changes, the medium porosity is recalculated at each time step. TOUGHREACT provides a variety of options for calculating permeability variation caused by mineral dissolution and precipitation. Some options only depend on changes in porosity, while others are formulas related to changes in fracture pore size and pore throat diameter. In this study, the cubic law (Equation (8)) was used to describe the relationship between permeability variation and porosity:

$$K = k_i \left( \frac{\varphi}{\varphi_i} \right)^3 \quad (8)$$

where  $k$  [m<sup>2</sup>] is the permeability; and  $k_i$  [m<sup>2</sup>] and  $\varphi_i$  are the initial permeability and porosity, respectively.

## 4. Model Establishment

### 4.1. Conceptual Model

This study aims to explore the laws of mineral dissolution and precipitation caused by fluid injection and their influencing mechanisms on the permeability of the near-well reservoir during the long-term operation of the EGS in the Matouying area. Multi-field coupling models of various minerals and hydrochemical components require massive calculations in the long-term simulation. Therefore, to effectively control the calculation time and improve the simulation efficiency, this study simplified the conceptual model and only simulated a 10 m thick monolayer in the water filtering interval of Well M-1. In addition, the fracture network in the artificial reservoir is mainly composed of dense small-scale fractures as revealed by the tracer test results of the Matouying EGS field (not published yet). Therefore, an equivalent porous medium was adopted in this study.

As shown in Figure 2, the model was established using the radial grid method (RZ2D) [30], with a vertical height of 10 m and a horizontal length of 200 m (i.e., the

distance between the injection well and the production well on site). Considering that the influence of the injected fluids on reservoirs gradually weakens with an increase in the distance from the injection well, the grid size gradually increased in the radial direction from the center of the model. The bottom of the model was set as an impermeable boundary with a constant temperature and pressure, and the injection well was set as the Dirichlet boundary to allow the flow rate to vary with time. In the process of simulation using TOUGHREACT, the grid volume of the matrix layers was set to infinity to make the matrix temperature and pressure constant. The permeability of the matrix layers was set to 0. This setting restricted the fluid exchange process between grids but did not affect the temperature and pressure transmission. Considering that some of the continuously injected fluids return to the surface through the production well and the remaining fluids flow toward distant strata and are lost during the long-term operation of the EGS, the outer boundary of the model was set as an infinite volume boundary. Based on the research results of Qi et al. [31], the temperature and pressure conditions of the model were set to 160 °C and 40 MPa, respectively.

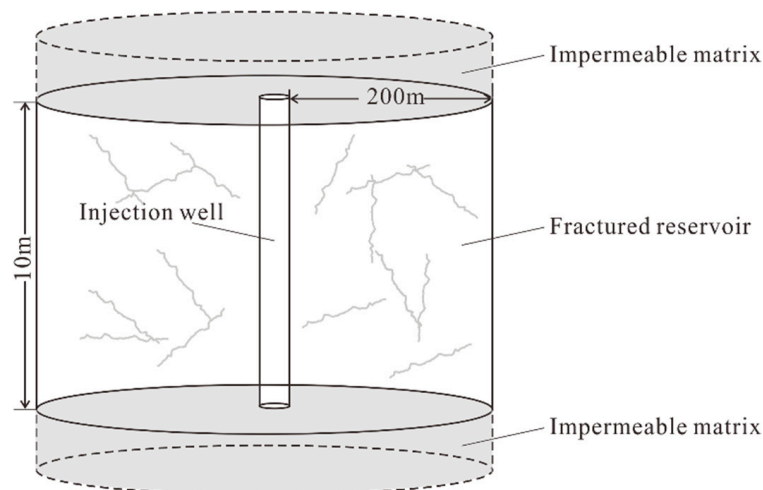


**Figure 2.** Conceptual model.

The chemical composition of the injected water and the rock mineral composition of the model were set according to the water-quality total-analysis data of the site and the XRD test results of rock samples, respectively [32]. The injected fluids were shallow groundwater extracted from the site and their main chemical compositions is shown in Table 1. The main minerals of the reservoir rocks included K-feldspar (30%), albites (33%), quartz (20%), chlorite (15%), and other trace minerals (2%).

**Table 1.** Main chemical composition of injected water.

Cation	Content (mg/L)	Proportion	Anion	Content (mg/L)	Proportion
K <sup>+</sup>	18.20	4.17%	F <sup>-</sup>	1.28	0.16%
Na <sup>+</sup>	225.49	51.71%	Cl <sup>-</sup>	295.03	36.86%
Ca <sup>2+</sup>	111.96	25.68%	NO <sub>3</sub> <sup>-</sup>	6.91	0.86%
Mg <sup>2+</sup>	31.48	7.22%	SO <sub>4</sub> <sup>-</sup>	169.41	21.16%
Fe <sup>2+</sup>	0.54	0.12%	HCO <sub>3</sub> <sup>-</sup>	327.86	40.96%
Zn <sup>2+</sup>	48.39	11.10%			

#### 4.2. Parameter Setting

The density, thermal conductivity, and specific heat capacity of the geothermal reservoir rocks were set according to the research data of the Matouying area [33], and the porosity and permeability were set according to the relevant numerical simulations [34]. The petrophysical parameters used in the model are shown in Table 2. It should be noted that

the porosity of the impermeable bedrock was not set to 0 but to a very low value compared to the reservoir porosity to prevent errors in the calculation process (e.g., a zero divisor). However, because the permeability was 0, this setting did not affect the flow and solute transport process in the reservoir grids.

**Table 2.** Petrophysical parameters.

Parameter	Value
Density (kg/m <sup>3</sup> )	2750.00
Porosity:	
Fractured reservoir	0.50
Impermeable matrix	0.01
Permeability (m <sup>2</sup> ):	
Fractured reservoir	$6.99 \times 10^{-14}$
Impermeable matrix	0
Thermal conductivity (W/kg·m)	2.20
Specific heat capacity (J/K·kg)	794.00

The dynamic reactions between minerals and the injected fluids were controlled using the parameters of mineral reaction kinetics. By referencing the numerical simulations of Na et al. [35] and Yang et al. [36], this study set the parameters of mineral reaction kinetics under different reaction mechanisms, as shown in Table 3.

**Table 3.** Parameters of mineral reaction kinetics.

Mineral	Neutral Mechanism		Acid Mechanism			Base Mechanism			A (cm <sup>2</sup> /g)
	K <sub>25</sub>	E	K <sub>25</sub>	E	n(H <sup>+</sup> )	K <sub>25</sub>	E	n(H <sup>+</sup> )	
	(mol/m <sup>2</sup> /s)	(KJ/mol)	(mol/m <sup>2</sup> /s)	(KJ/mol)		(mol/m <sup>2</sup> /s)	(KJ/mol)		
Quartz	$1.203 \times 10^{-14}$	87.70							9.8
K-f × 10ldspar	$3.890 \times 10^{-13}$	38.00	$8.710 \times 10^{-11}$	51.70	0.500	$6.310 \times 10^{-12}$	94.10	−0.823	9.8
Albit × 10	$2.754 \times 10^{-13}$	69.80	$6.918 \times 10^{-11}$	65.00	0.457	$2.512 \times 10^{-16}$	71.00	−0.572	9.8
Chlorit × 10	$3.020 \times 10^{-13}$	88.00	$7.762 \times 10^{-12}$	88.00	0.500				151.6
Montmor-Na	$1.660 \times 10^{-13}$	35.00	$1.047 \times 10^{-11}$	23.60	0.340	$3.020 \times 10^{-17}$	58.90	−0.400	151.6
Montmor-Ca	$1.660 \times 10^{-13}$	35.00	$1.047 \times 10^{-11}$	23.60	0.340	$3.020 \times 10^{-17}$	58.90	−0.400	151.6
Illit × 10	$1.660 \times 10^{-13}$	35.00	$1.047 \times 10^{-11}$	23.60	0.340	$3.020 \times 10^{-17}$	58.90	−0.400	151.6
Calcit × 10	$1.550 \times 10^{-16}$	23.50	$6.018 \times 10^{-13}$	14.40	1.000				9.8
Kaolinit × 10	$6.918 \times 10^{-14}$	22.20	$4.898 \times 10^{-12}$	65.90	0.777	$8.913 \times 10^{-18}$	17.90	−0.472	151.6
Montmor-Mg	$1.660 \times 10^{-13}$	35.00	$1.047 \times 10^{-11}$	23.60	0.340	$3.020 \times 10^{-17}$	58.90	−0.400	151.6
Montmor-K	$1.660 \times 10^{-13}$	35.00	$1.047 \times 10^{-11}$	23.60	0.340	$3.020 \times 10^{-17}$	58.90	−0.400	151.6
Dolomit × 10	$2.951 \times 10^{-8}$	52.20	$6.457 \times 10^{-4}$	36.10	0.500				9.8
Dawsonit × 10	$1.260 \times 10^{-9}$	62.76	$6.457 \times 10^{-4}$	36.10	0.500				9.8
Sid × 10rit × 10	$1.260 \times 10^{-9}$	62.76	$6.457 \times 10^{-4}$	36.10	0.500				9.8
Magn × 10sit × 10	$4.508 \times 10^{-11}$	23.50	$4.169 \times 10^{-11}$	14.40	1.000				9.8
H × 10matit × 10	$2.512 \times 10^{-15}$	66.20	$4.074 \times 10^{-10}$	66.20	1.000				9.8

#### 4.3. Simulation Schemes

To explore the laws of the influences of key operating parameters (i.e., injection flow rate, injection temperature, and hydrochemical composition) on the mineral dissolution and precipitation and the permeability variation of the near-well reservoir, this study designed and operated multiple simulation schemes according to the actual situation of the site and the results from hydrochemical analysis and testing, as shown in Table 4 and Figure 3. The injection flow rate was set to 3 m<sup>3</sup>/h, 4 m<sup>3</sup>/h, 5 m<sup>3</sup>/h, and 6 m<sup>3</sup>/h in the simulation schemes (approximately equivalent to the injection flow rate of 90 m<sup>3</sup>/h, 120 m<sup>3</sup>/h, 150 m<sup>3</sup>/h, and 180 m<sup>3</sup>/h in the entire water filtering interval, respectively). In the injection process, the changes in wellhead injection temperature and wellbore heat loss affect the temperature of injection fluids when the fluids enter the reservoir. Therefore, the injection temperature was set to 50 °C, 70 °C, and 90 °C. It is noteworthy that the injection temperatures set in the simulations were the temperatures when the fluid flowed into the

reservoir through the injection wellbore rather than the temperatures when fluids were injected from the surface.

**Table 4.** Simulation schemes of different injection flow rates and temperatures.

Scheme No.	Injection Flow Rate (m <sup>3</sup> /h)	Injection Temperature (°C)
1	3	70
2	4	70
3 (Basic Scheme)	5	70
4	6	70
5	5	90
6	5	50

When designing different chemical composition schemes of injected water, the contents of three main metal ions (K<sup>+</sup>, Ca<sup>2+</sup>, and Mg<sup>2+</sup>) were adjusted to replace the proportion of Na<sup>+</sup> in the metal cations of the basic scheme. Based on this, the hydrochemical equilibrium of the injected water was adjusted and recalculated. The specific settings of chemical components of the injected water in different schemes are shown in Figure 3.

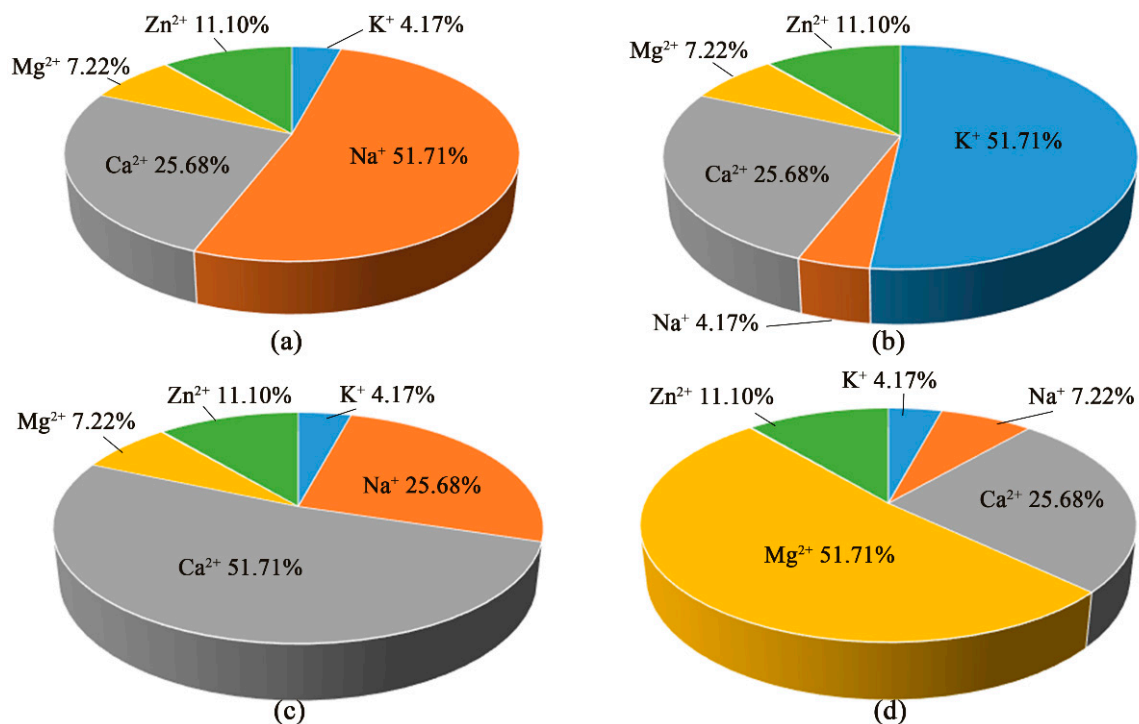


**Figure 3.** Simulation schemes for different chemical compositions of injected water. (a)—Basic scheme; (b)—Scheme 7; (c)—Scheme 8; (d)—Scheme 9.

## 5. Results and Discussion

### 5.1. Changes at Different Distances from the Injection Well

The changes in the reservoir porosity and permeability and initial mineral contents at different distances from the injection well after continuous injection for 10 a are shown in Figure 4. As shown in Figure 4a, after 10 a of continuous operation of the EGS, significant changes in porosity and permeability mainly occurred approximately 0–7.5 m away from the injection well. In a range within 3.5 m from the well, the reservoir porosity and permeability decreased significantly, reflecting strong precipitation of secondary minerals in this range. The decreased amplitude increased as the distance from the injection well decreased, indicating that the intensity of water-rock interactions decreased with an increase in the distance. At 10 a, the porosity at the injection well decreased by 60.0% from the



initial value of 0.5 to 0.2, and the permeability decreased by 94.1% from  $6.99 \times 10^{-14} \text{ m}^2$  to  $4.15 \times 10^{-15} \text{ m}^2$ , indicating that the long-term operation of geothermal wells seriously damaged the permeability of the near-well artificial reservoir. It should be noted that the reservoir permeability within the range of 3.5–7.5 from the injection point was slightly higher than its initial value, suggesting that the porosity increase caused by the initial mineral dissolution was more intense than the permeability decrease caused by the secondary mineral precipitation, as further discussed below.

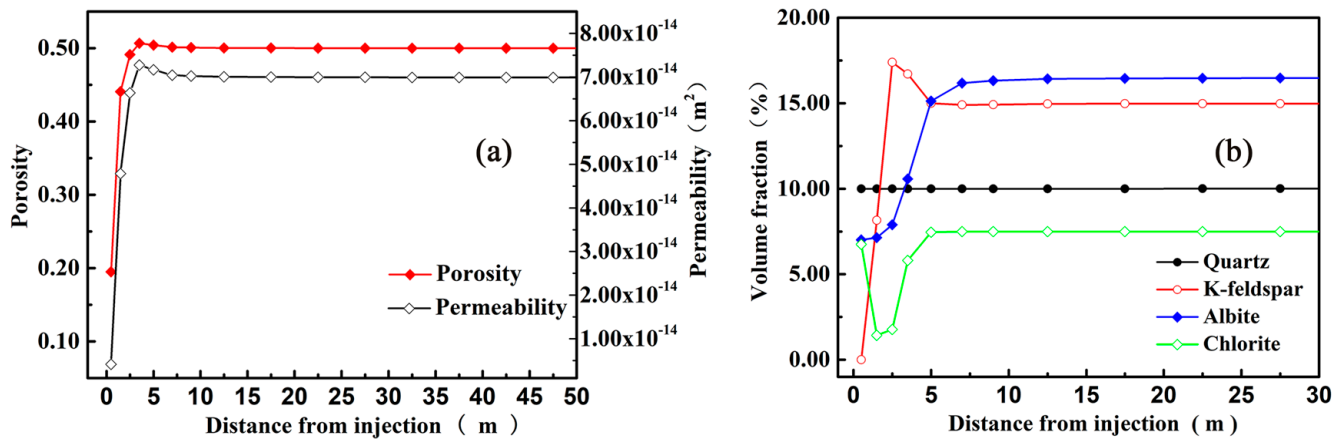
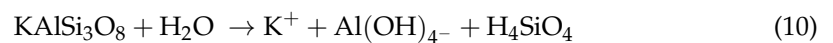
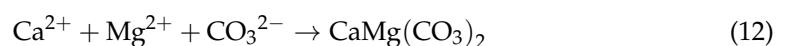


**Figure 4.** Simulation results at different distances from the injection point. (a)—Porosity and permeability; (b)—Content of primary minerals.

As shown in Figure 4b, the content of primary quartz in the reservoir scarcely changed during the long-term injection, while the K-feldspar, albite, and chlorite contents changed to varying degrees, reflecting that the injected fluids had a significant effect on the dissolution of the three primary minerals (Equations (9)–(11)). The albite and chlorite contents were lower than their initial values 5–7 m away from the injection well. The K-feldspar content decreased significantly 0–2.5 m away from the injection well but was higher than its initial value in the range of 2.5–7.5 m from the well, reflecting the severe dissolution of K-feldspar near the injection well and the formation of secondary K-feldspar, respectively. This changing trend is consistent with the research results of Zhao et al. [22].



The global secondary mineral generation at 10 a is shown in Figure 5. According to this figure, a variety of secondary minerals set in the model were generated to different degrees. Among them, illite and dolomite showed the most significant secondary precipitation, especially near the injection point (within the range of about 5 m), and the volume fraction of their precipitation reached the same order of magnitude as their initial content. Therefore, they had a far greater impact on reservoir porosity and permeability than other secondary minerals. The main reason for a large quantity of secondary dolomite is that the injected fluid contained a lot of  $\text{Ca}^{2+}$  and  $\text{HCO}_3^-$ , in which  $\text{HCO}_3^-$  decomposed at a high temperature to produce  $\text{CO}_3^{2-}$  or was combined with  $\text{Ca}^{2+}$  and  $\text{Mg}^{2+}$  to form dolomite precipitation (Equation (12)). In addition, the chlorite dissolution (Equation (11)) also provided more sufficient  $\text{Mg}^{2+}$ . The illite formation was mainly controlled by feldspar minerals, especially  $\text{K}^+$  and other components provided by the K-feldspar dissolution.



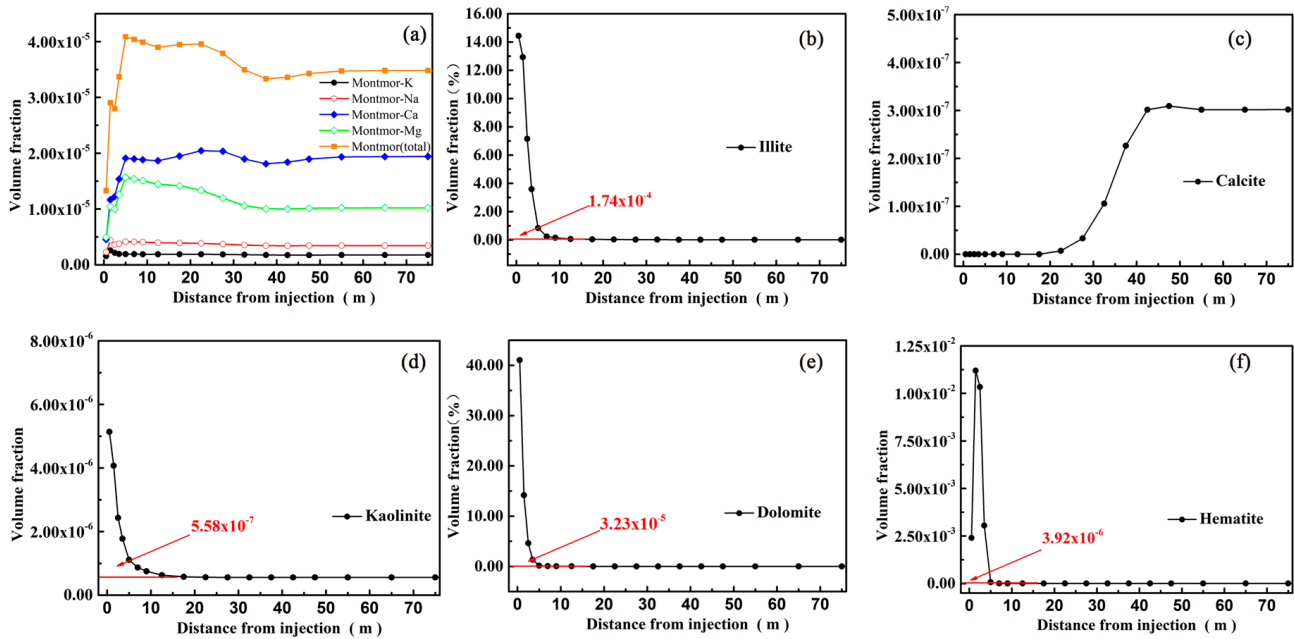
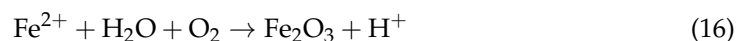
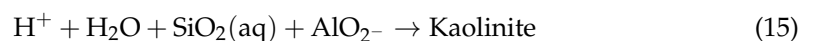
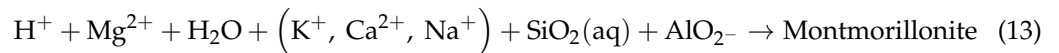


**Figure 5.** Precipitation of secondary minerals. (a)—Montmorillonite; (b)—Illite; (c)—Calcite; (d)—Kaolinite; (e)—Dolomite; (f)—Hematite.

In sum, significant changes in the porosity and permeability of the near-well reservoir were mainly caused by the dissolution of the initial minerals (K-feldspar, albite, and chlorite) and the secondary precipitation of dolomite and illite. In fact, secondary minerals were generated in the whole reservoir, but they had no significant impact on the reservoir permeability far away from the injection well due to their very low contents. The production of montmorillonite (Equation (13)), calcite (Equation (14)), and kaolinite (Equation (15)) was all below  $1 \times 10^{-4}$ . By contrast, the production of hematite (Equation (16)) was slightly higher, but its highest value near the injection point was only 1.1% of the initial content. Figure 5a shows the total amount of produced montmorillonite and the amounts of the four types of montmorillonite produced. According to this figure, the secondary montmorillonite mainly included calcium montmorillonite and magnesium montmorillonite. The production of montmorillonite and calcite near the injection point was lower than that in the far-well zones. This result is different from the changing trend that the production of other secondary minerals decreased with an increase in the distance from the injection point. This phenomenon occurred because  $\text{Ca}^{2+}$ ,  $\text{Mg}^{2+}$ , and  $\text{HCO}_3^-$  were preferentially consumed to form dolomite and illite but the fluid flow and solute transport caused by the injection inhibited the precipitation of montmorillonite and calcite.



During the actual operation of the EGS, the process of particle migration (the precipitation of both primary and secondary minerals) caused by fluid injection, as well as the spatial heterogeneity of fracture distribution and scale, may cause suspended particle plugging and distant reservoir. This study simplified the actual conditions without considering this process. However, it is significant to improve the calculation code to include this process in the subsequent work.

### 5.2. Changes at Injection Point

As concluded from the analysis of the global monitoring results at 10 a of the model, the mineral dissolution and precipitation and the significant changes in the reservoir porosity and permeability mainly occurred near the injection point because of the drastic changes in temperature, flow field, and hydrochemical composition caused by the injection of cold water. Therefore, it is necessary to monitor and analyze the reservoir porosity and permeability at the injection grid, as well as the changes in the mineral dissolution and precipitation with time during the injection. The results are shown in Figure 6.

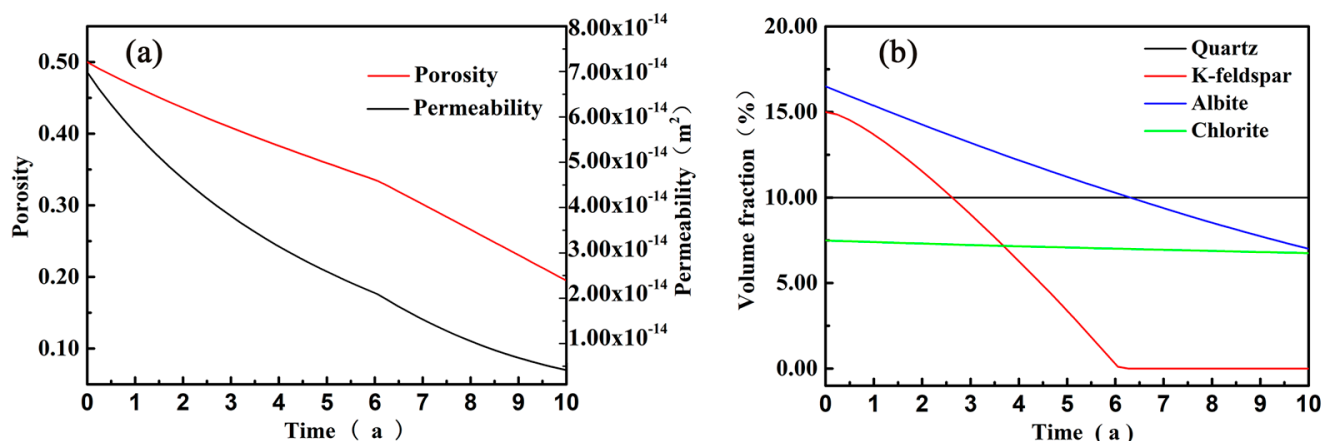
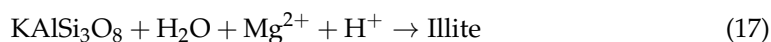


**Figure 6.** Time-varying simulation results at the injection point. (a)—Porosity and permeability; (b)—Primary minerals.

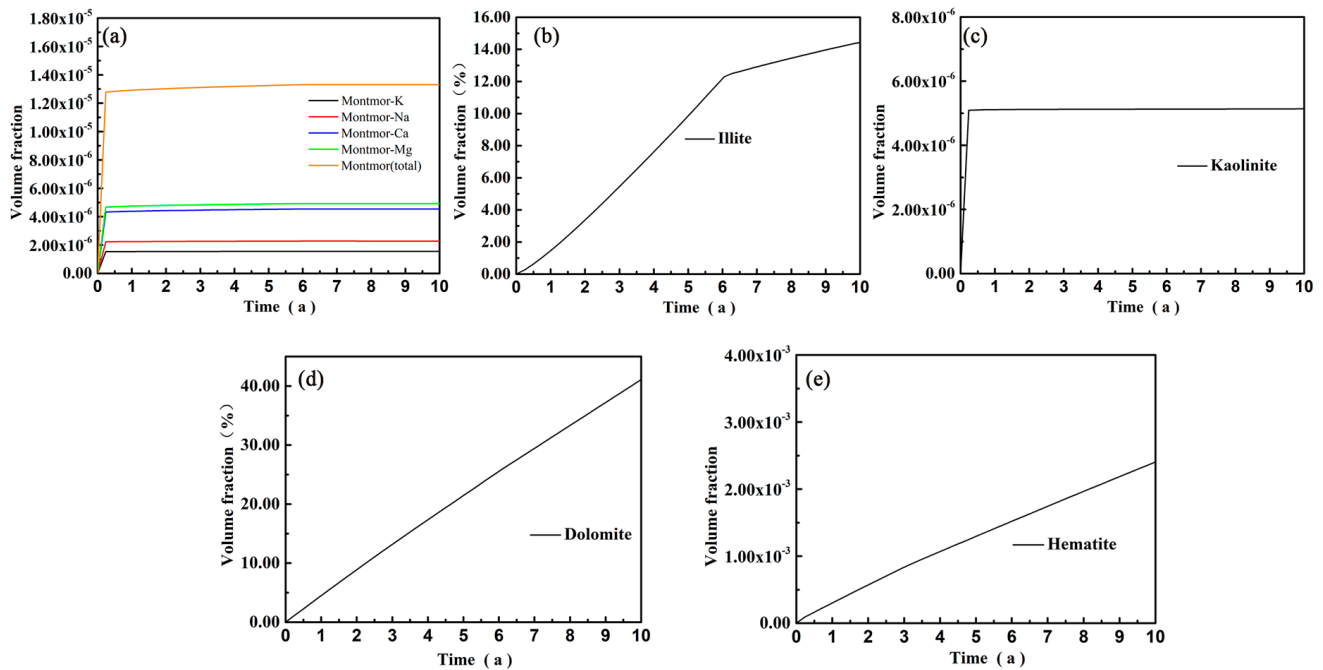
As shown in Figure 6, the reservoir porosity and permeability at the injection point decreased continuously as the injection continued, even at 10 a. The injected water yielded the most significant and rapid effect on the K-feldspar dissolution. The effect was intensified as the injection continued, and the K-feldspar completely dissolved by 6 a. The albite and chlorite contents decreased at stable rates, and the chlorite content decreased gently. As shown in Figure 4b, the injected water was more conducive to the dissolution of feldspar minerals, especially K-feldspar.

Figure 7 shows the formation of various secondary minerals at the injection point during the whole operation of the EGS (no calcite was formed for the reasons discussed above, and therefore no calcite is shown in these figures). As shown in Figure 7, the montmorillonite and kaolinite contents only increased continuously in the first 6 months and then were almost stabilized. Their final precipitate quantities were only approximately  $1.28 \times 10^{-5}$  and  $5.10 \times 10^{-6}$ , respectively, which cannot affect the reservoir porosity and permeability. The illite, dolomite, and hematite contents continuously increased during the whole operation of the EGS, and the precipitate quantity of hematite was small and was only  $2.40 \times 10^{-3}$  at 10 a. The generation rate of illite decreased significantly after 6 a. This occurred because the primary K-feldspar was almost all dissolved near the injection point with the continuous progress of fluid injection and solute transport (Figures 4b and 6b), and thus the main  $\text{K}^+$  source for the illite formation was lost. According to the analysis in Section 5.1, the illite precipitation was mainly controlled by the dissolution of feldspar minerals, especially K-feldspar. This conclusion is consistent with the analysis results of Xue et al. [37]. Based on the relevant literature, the transformation of  $\text{K}^+$  from K-feldspar to illite can be summarized as Equation (17). At 10 a, the illite content at the injection point reached 14.4%.



The dolomite precipitation in the whole injection process (the dolomite content reached 41.0% at 10 a) was the main reason for the significant decrease in the reservoir porosity and permeability at the injection point. The continuous and rapid dolomite formation

was attributable to the continuous injection of fluids containing  $\text{Ca}^{2+}$ ,  $\text{Mg}^{2+}$ , and  $\text{HCO}_3^-$ . Moreover, the dissolution of the initial mineral chlorite can also provide sufficient  $\text{Mg}^{2+}$ .



**Figure 7.** Precipitation of secondary minerals at the injection point. (a)—Montmorillonite; (b)—Illite; (c)—Kaolinite; (d)—Dolomite; (e)—Hematite.

Overall, the water–rock interactions in the fluid injection process led to the dissolution of primary minerals and the formation of massive secondary minerals, leading to a continuous decrease in the permeability of the near-well reservoir. The intuitive effect of this process on the EGS operation was mainly reflected in the continuous increase in the injection pressure. To further explore the process, the simulation time of the basic scheme was set to 30 a, and the changes in the permeability at the injection grid and fluid pressure over time were monitored. Considering that the plugging process of the reservoir in this study is affected by the selected calculation method for the change in permeability, the calculation method in the original case was changed from the cubic law to the simplified Carman–Kozeny relation (18), and the simulation results (Figure 8) were compared with the original results to further analyze the effect.

$$k = k_i \left( \frac{\varphi}{\varphi_i} \right)^3 \frac{(1 - \varphi_i)^2}{(1 - \varphi)^2} \quad (18)$$

As shown in Figure 8, the fluid pressure at the injection grid gradually increased in the long-term injection process with a decrease in the permeability. The fluid pressure increased slowly and stably within the first 10 a and increased sharply after 10 a. At about 12 a, the reservoir permeability at the injection grid was lower than  $3.00 \times 10^{-16} \text{ m}^2$  and the fluid pressure rose rapidly in a short time. Therefore, it is considered that the injection grid was plugged at this time. In the actual production process, once the injection pressure exceeds the threshold that the equipment withstands, the injection cannot be sustained. Considering that the operating life of an EGS is generally expected to be 20–30 a, it is necessary to reasonably control the injection flow rate, injection temperature, and hydrochemical composition during the long-term operation and regularly perform chemical treatments to remove the well plugging, aiming to mitigate the damage to the permeability of the near-well reservoir caused by water–rock interactions. Compared with the case using the cubic law, the simulation results obtained using the Carman–Kozeny relation showed a certain gap in the changes in the permeability and fluid pressure at the

injection grid. Specifically, the permeability was lower than that of the original plan during the whole injection period. The differences in fluid pressure were not apparent in the early stage (about 7 years) and then gradually increased, with the growth rate increasing sharply. Therefore, in this case, plugging occurred earlier than that in the original scheme (less than 1 a). The possible reason is that the reservoir permeability is more sensitive to porosity changes in the Carman–Kozeny relation, which should be more applicable to porous reservoirs with low permeability. In conclusion, the use of different relations for the change in reservoir permeability has a certain impact on the evolutionary process of plugging but does not change the occurrence and form of plugging.

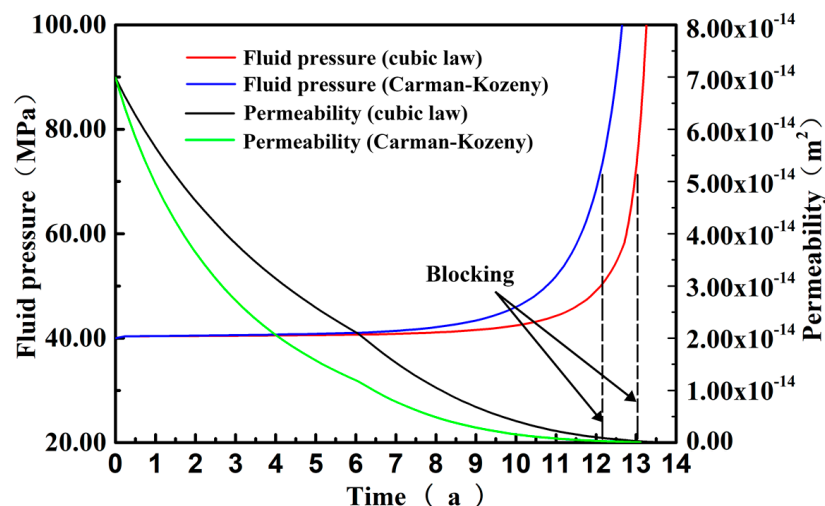
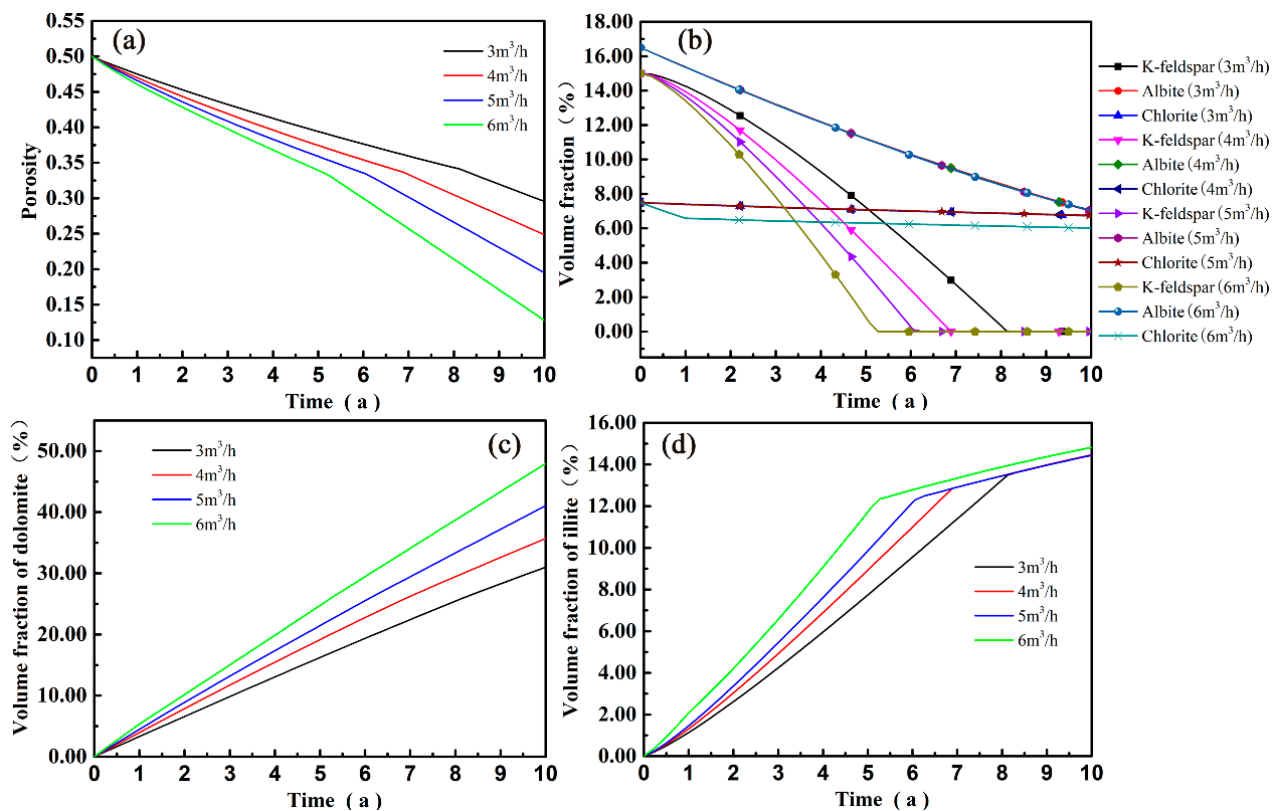


Figure 8. Changes in the permeability and pressure at the injection grid.

### 5.3. Sensitivity Analysis

#### 5.3.1. Influence of Different Injection Flow Rates

Figure 9 shows the time-varying changes in the porosity of the injection grid, the initial mineral contents, and the contents of main secondary minerals under different injection flow rates and an injection temperature of 70 °C. As the injection flow rate increased, the porosity at the injection point decreased more significantly during the same operation time for two reasons. First, a higher injection flow rate destructed the chemistry equilibrium of the near-well water more significantly, driving the chemical reactions to develop toward the formation of secondary minerals. Second, a higher injection flow rate intensified the dissolution of primary minerals, providing more sufficient material sources for the formation of secondary minerals. The different effects of different injection flow rates on the initial mineral contents were mainly reflected in the K-feldspar dissolution. As shown in Figure 9b, K-feldspar dissolved more rapidly and reached equilibrium in a shorter time under a higher flow rate, leading to a higher formation rate of illite in the early operation stage of the EGS (when K-feldspar was not completely dissolved; Figure 9d). The illite content did not change significantly in the late operation stage of the EGS when the injection flow rate was set to below 5 m<sup>3</sup>/h and only increased when the flow rate reached 6 m<sup>3</sup>/h. In conclusion, the illite formation was mainly controlled by the K-feldspar dissolution. Both the formation rate and total quantity of dolomite increased significantly with an increase in the injection flow rate, and the formation rates of dolomite under different schemes tended to be stable. These results reflect that the Mg<sup>2+</sup> content in the system was sufficiently high and the dolomite precipitation was mainly controlled by the injected Ca<sup>2+</sup> and HCO<sub>3</sub><sup>−</sup>.



**Figure 9.** Simulation results at different injection flow rates. (a)—Porosity; (b)—Permeability; (c)—Dolomite; (d)—Illite.

### 5.3.2. Influence of Different Injection Temperatures

Figure 10 shows the time-varying changes in the porosity of the injection grid, the initial mineral contents, and the contents of main secondary minerals under different injection temperatures and an injection flow rate of 5 m<sup>3</sup>/h. During the initial injection within the first 3 a, there was no significant difference in the porosity at the injection point under different injection temperatures. The porosity at the injection point during the first 3–5.4 a under an injection temperature of 90 °C was significantly higher than that of the other two schemes. This occurred because the increase in the injection temperature expedited the initial mineral dissolution, effectively counteracting the plugging effect of secondary mineral formation in the near-well reservoir. As shown in Figure 10b, the dissolution rates of K-feldspar and albite significantly increased with an increase in the injection temperature, while the dissolution rate of chlorite only slightly changed when the injection temperature increased from 50 °C to 70 °C and then increased significantly when the injection temperature increased to 90 °C. The differences in porosity between different schemes increased gradually in the late injection stage, and the porosity at the injection point decreased with an increase in the injection temperature. The reason for this trend is that with a decrease in initial mineral contents in the late injection stage, the increase in the reservoir porosity caused by initial mineral dissolution gradually weakened, but secondary minerals were formed continuously. As shown in Figure 10c,d, the formation quantities and rates of dolomite and illite both increased with an increase in the injection temperature, while the formation rate of illite decreased with an increase in the injection temperature after the turning point (note: the turning point appeared increasingly earlier with an increase in the injection temperature, and there was a significant correlation between its appearance time and the K-feldspar dissolution). This occurred because the main K<sup>+</sup> source was lost after the complete dissolution of K-feldspar and more Mg<sup>2+</sup> was consumed by the dolomite precipitation.

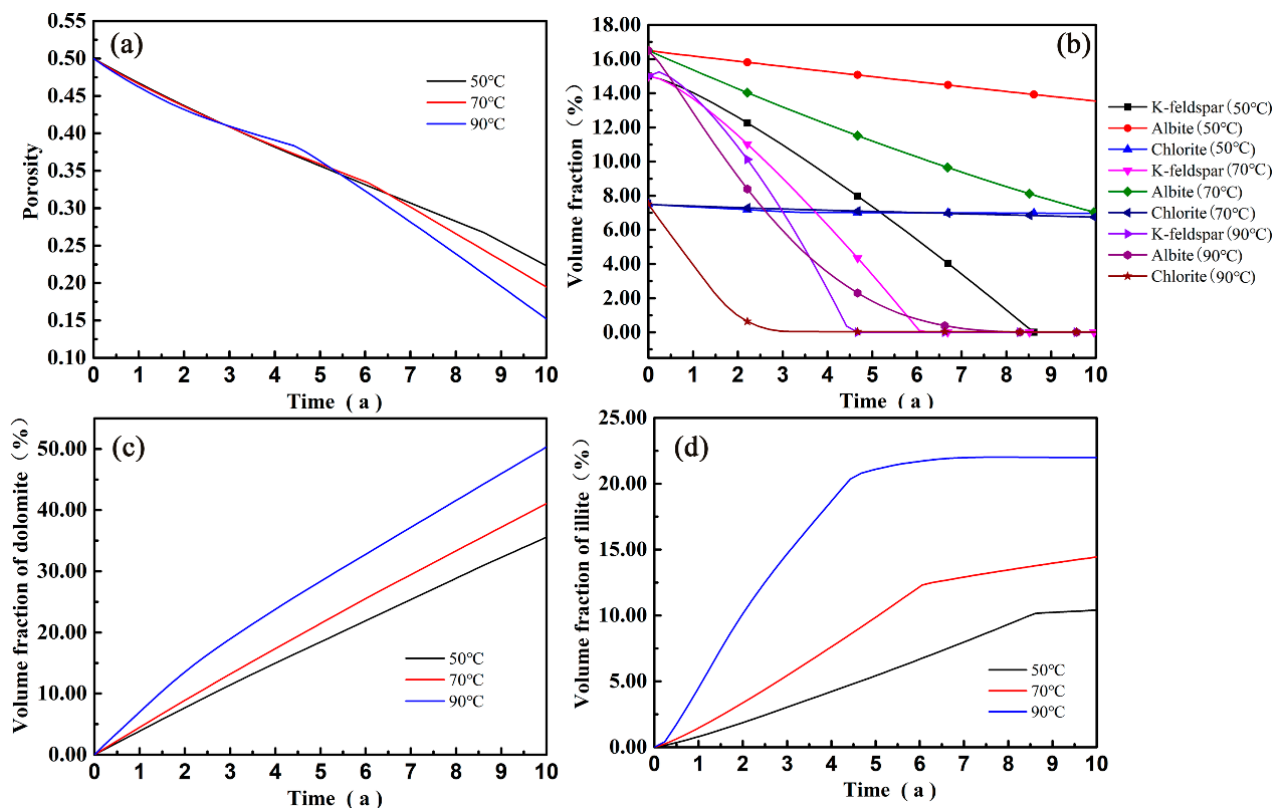


**Figure 10.** Simulation results at different injection temperatures. (a)—Porosity; (b)—Permeability; (c)—Dolomite; (d)—Illite.

### 5.3.3. Influence of Different Hydrochemical Compositions

Figure 11 shows the simulation results of different chemical composition schemes of injected water under an injection flow rate of  $5 \text{ m}^3/\text{h}$  and an injection temperature of  $70^\circ\text{C}$ . Compared to the basic scheme, the porosity at the injection point in different chemical composition schemes decreased to different degrees. Among them, the porosity in Scheme 8 ( $\text{Ca}^{2+}$  was the leading cation) decreased slightly, while the porosity in Scheme 7 ( $\text{K}^+$  was the leading cation) decreased to below 0.05 at 7a. In this case, the fluid pressure at the injection grid was too high to ensure continuous and stable injection. In Scheme 9 ( $\text{Mg}^{2+}$  was the leading cation), a substantial decrease in the porosity appeared at 4a. Therefore, it can be preliminarily determined that  $\text{Mg}^{2+}$  had the most significant influence on the porosity and permeability of the near-well reservoir in the study area.

Changes in the chemical composition of injected water have different degrees of effects on the dissolution of initial minerals and the generation of secondary minerals. The dissolution of initial minerals in Scheme 7 was most significantly different from that in the basic scheme. The high increase in the  $\text{K}^+$  concentration in this scheme inhibited the dissolution of primary K-feldspar and led to the formation of massive secondary K-feldspar (Figure 11b). This process and the sharp decrease in the  $\text{Na}^+$  concentration greatly promoted the albite and chlorite dissolution (Figure 11c,d), thus providing more sufficient  $\text{Mg}^{2+}$  for the dolomite formation (Figure 11e). In addition, since no K-feldspar dissolved in Scheme 7 and the  $\text{K}^+$  in the injected fluid was mainly consumed by the formation of secondary K-feldspar, the illite formation was inhibited and the precipitate quantity of illite was only  $3.96 \times 10^{-4}$  at 7a. The influence of the increase in the  $\text{Mg}^{2+}$  concentration on the mineral contents in Scheme 9 was mainly reflected in the formation of secondary minerals. As shown in Figure 11e,f, the generation rates of dolomite and illite significantly increased compared with other schemes. In Scheme 9, as illite continued to be formed and the chlorite dissolution gradually reached equilibrium in the late injection stage, the

K-feldspar dissolution intensified, releasing a large amount of  $K^+$  and  $Mg^{2+}$  and further increasing the formation rate of the two main secondary minerals, i.e., illite and chlorite.

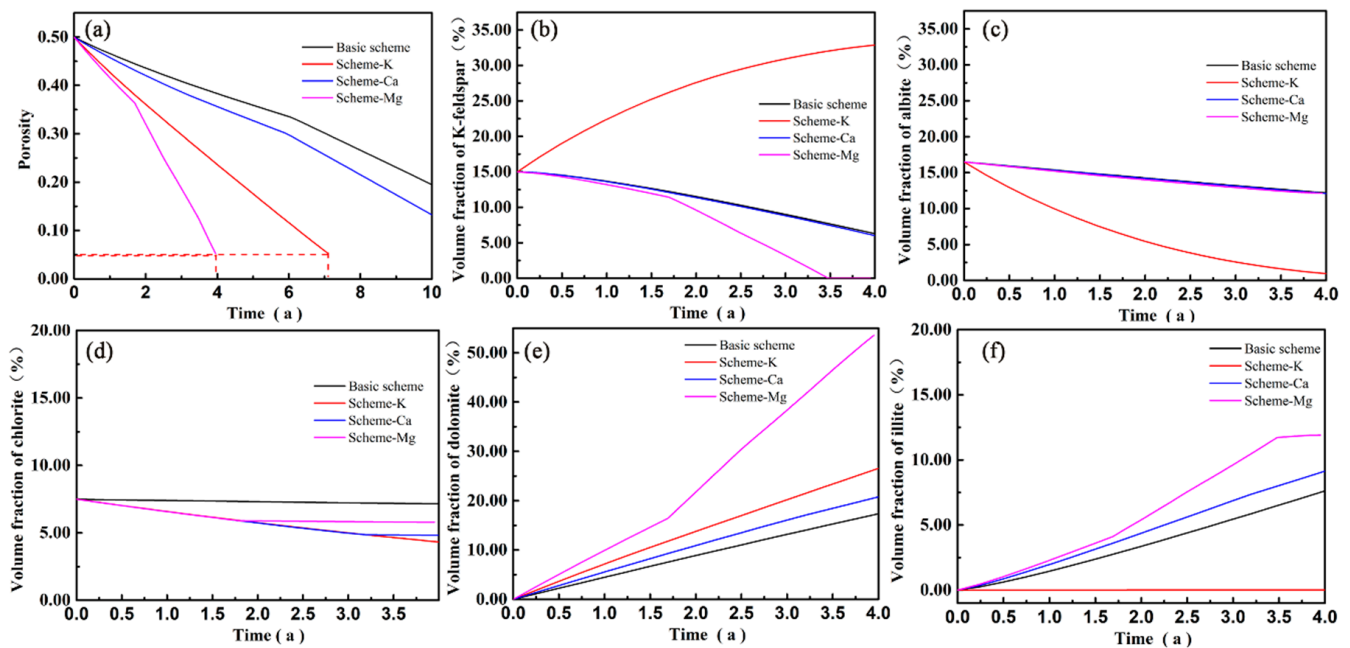


**Figure 11.** Simulation results under different hydrochemical compositions. (a)—Porosity; (b)—K-Feldspar; (c)—Albite; (d)—Chlorite; (e)—Dolomite; (f)—Illite.

In sum,  $Mg^{2+}$  and  $K^+$  have the most significant effects on mineral dissolution and precipitation and the permeability of the near-well reservoir among the chemical components in injected water. Therefore, it is necessary to control the  $Mg^{2+}$  and  $K^+$  contents by adding metal ion chelating agents and corrosion inhibitors to the injected water in the long-term operation of geothermal wells.

## 6. Conclusions

Based on the investigation of Well M-1 in the EGS in the Matouying uplift of Hebei Province, China, this study established a THC reactive solute transport model using the TOUGHREACT program. Using this model, this study explored the mineral dissolution and precipitation laws of the near-well reservoir and their influencing mechanisms on reservoir porosity and permeability in the long-term injection process of this well and analyzed the effects of different injection conditions (injection flow rate, injection temperature, and hydrochemical composition) on the injection process. The conclusions are as follows.

(1) A significant decrease in the porosity and permeability of the EGS reservoir in the Matouying uplift occurred 0–7.5 m away from Well M-1 in the long-term injection process. At 10 a, the porosity at the injection point decreased by 60.0% and the permeability decreased by 94.2%. This occurred due to the dissolution of primary K-feldspar, albite, and chlorite and the formation of secondary minerals dominated by dolomite and illite.

(2) The decreasing rates of the permeability and the porosity of the near-well reservoir in the EGS of the Matouying uplift increased with an increase in the injection flow rate. The reason is that a higher injection flow rate expedited the dissolution of primary K-feldspar, thus providing more sufficient ions for the formation of secondary minerals and promoting the formation of dolomite and illite.

(3) In this simulation, the change in the injection temperature had significant effects on the dissolution of primary minerals and the precipitation of main secondary minerals. Moreover, it had a slight influence on the variation trends of the porosity and permeability of the near-well reservoir in the early injection stage. However, with a decrease in the primary mineral content and the continuous formation of secondary minerals, the decreasing rates



of the porosity and permeability of the near-well reservoir significantly increased with an increase in the injection temperature.

(4) The increase in the  $K^+$  and  $Mg^{2+}$  contents in the main chemical components of the injected water expedited the precipitation of dolomite and illite and further greatly exacerbated the plugging of the near-well reservoir in the EGS of the Matouying uplift. Therefore, to improve the operating life of the EGS, it is absolutely necessary to control the content of metal ions, especially  $K^+$  and  $Mg^{2+}$ , in the injected water during the long-term injection.

**Author Contributions:** Conceptual model and numerical simulation, B.F. and Z.C.; visualization and writing, X.L.; sample collection and data acquisition, S.S. and X.Q.; funding acquisition and resource administration, S.L. All authors have read and agreed to the published version of the manuscript.

**Funding:** This work was supported by the National Key R&D Program of China (No. 2018YFB1501802), the S&T Program of Hebei Provincial (No. 20374201D), the Chinese Academy of Geological Sciences Fund (No. SK202104), the Jilin Provincial Department of Science and Technology (No. 20200403147SF), the Academician Workstation and Academician Cooperation Key Unit Construction of the Second Geological Team of Hebei Coal Geology Bureau (No. 205A4101H), and the research and application demonstration of single-well heat recovery technology and ground comprehensive heat utilization technology for the thermal energy of dry hot rocks (No. 19274102D).

**Institutional Review Board Statement:** Not applicable.

**Informed Consent Statement:** Not applicable.

**Data Availability Statement:** The original contributions presented in the study are included in the article, and further inquiries can be directed to the corresponding author.

**Acknowledgments:** The authors would like to extend their sincere gratitude to the relevant institutions for financial and technical support.

**Conflicts of Interest:** The authors declare no conflict of interest.

## References

1. Soltani, M.; Kashkooli, F.M.; Dehghani-Sanij, A.R.; Kazemi, A.R.; Bordbar, N.; Farshchi, M.J.; Elmi, M.; Gharali, K.; Dusseault, M.B. A comprehensive study of geothermal heating and cooling systems. *Sustain. Cities Soc.* **2019**, *44*, 793–818. [[CrossRef](#)]
2. Hu, X.; Lv, J.; Li, S.; Du, G.; Wang, Z.; Li, H.; Zhu, H. Joint interpretation technology of favorable HDR geothermal resource exploration in Northern Songliao Basin. *Unconv. Resour.* **2022**, *2*, 133–138. [[CrossRef](#)]
3. Rathnaweera, T.D.; Wu, W.; Ji, Y.; Gamage, R.P. Understanding injection-induced seismicity in enhanced geothermal systems: The coupled thermo-hydro-mechanical-chemical process to anthropogenic earthquake prediction. *Earth-Sci. Rev.* **2020**, *205*, 103182. [[CrossRef](#)]
4. Wang, D.; Dong, Y.; Li, Y.; Wang, Y.; Li, Y.; Liu, H.; Zhang, W.; Sun, D.; Yu, B. Numerical simulation of heat recovery potential of hot dry rock under alternate temperature loading. *Unconv. Resour.* **2022**, *2*, 170–182. [[CrossRef](#)]
5. Kharseh, M.; Al-Khawaja, M. Optimizing Geothermal Energy Resource. *Mech. Eng. Autom.* **2015**, *5*, 667–675.
6. Barcelona, H.; Senger, M.; Yagupsky, D. Resource assessment of the Copahue geothermal field. *Geothermics* **2021**, *90*, 101987. [[CrossRef](#)]
7. El Bouazouli, A.; Baidder, L.; Diagana, O.; Rhoulzlane, S.; Bichri, A. Prospecting of potential geothermal resources from the east to the Moroccan Sahara. *Mater. Today Proc.* **2020**, *27*, 3224–3233. [[CrossRef](#)]
8. Olasolo, P.; Juárez, M.C.; Morales, M.P.; D'Amico, S.; Liarte, I.A. Enhanced geothermal systems (EGS): A review. *Renew. Sustain. Energy Rev.* **2016**, *56*, 133–144. [[CrossRef](#)]
9. Alegria, P.; Catalan, L.; Araiz, M.; Rodriguez, A.; Astrain, D. Experimental development of a novel thermoelectric generator without moving parts to harness shallow hot dry rock fields. *Appl. Therm. Eng.* **2022**, *200*, 117619. [[CrossRef](#)]
10. Lv, Y.; Yuan, C.; Zhu, X.; Gan, Q.; Li, H. THMD analysis of fluid injection-induced fault reactivation and slip in EGS. *Geothermics* **2022**, *99*, 102303. [[CrossRef](#)]
11. Asai, P.; Podgorney, R.; McLennan, J.; Deo, M.; Moore, J. Analytical model for fluid flow distribution in an Enhanced Geothermal Systems (EGS). *Renew. Energy* **2022**, *193*, 821–831. [[CrossRef](#)]
12. Borgia, A.; Pruess, K.; Kneafsey, T.J.; Oldenburg, C.M.; Pan, L. Simulation of  $CO_2$ -EGS in a Fractured Reservoir with Salt Precipitation. *Energy Procedia* **2013**, *37*, 6617–6624. [[CrossRef](#)]
13. Driba, D. 1D Thermal-Hydraulic-Chemical (THC) Reactive transport modeling for deep geothermal systems: A case study of Groß Schönebeck reservoir, Germany. In *Agu Fall Meeting*; American Geophysical Union: San Francisco, CA, USA, 2014.
14. Ren, G.; Jiang, J.; Younis, R.M. A Model for Coupled Geomechanics and Multiphase Flow in Fractured Porous Media Using Embedded Meshes. *Adv. Water Resour.* **2018**, *122*, 113–130. [[CrossRef](#)]

15. Salimzadeh, S.; Paluszny, A.; Nick, H.M.; Zimmerman, R.W. A Three-Dimensional Coupled Thermo-Hydro-Mechanical Model for Deformable Fractured Geothermal Systems. *Geothermics* **2017**, *71*, 212–224. [[CrossRef](#)]
16. Pei, Y.; Sepehrmoori, K. Efficient Modeling of Depletion Induced Fracture Deformation in Unconventional Reservoirs. In Proceedings of the SPE Annual Technical Conference and Exhibition, Dubai, United Arab Emirates, 21–23 September 2021. [[CrossRef](#)]
17. Li, T.; Han, D.; Yang, F.; Li, J.; Wang, D.; Yu, B.; Wei, J. Modeling Study of the Thermal-Hydraulic-Mechanical Coupling Process for EGS Based on the Framework of EDFM and XFEM. *Geothermics* **2022**, *89*, 101953. [[CrossRef](#)]
18. Yuan, Y.; Xu, T.; Moore, J.; Lei, H.; Feng, B. Coupled Thermo–Hydro–Mechanical Modeling of Hydro-Shearing Stimulation in an Enhanced Geothermal System in the Raft River Geothermal Field, USA. *Rock Mech. Rock Eng.* **2020**, *53*, 5371–5388. [[CrossRef](#)]
19. Regenspurg, S.; Feldbusch, E.; Byrne, J.; Deon, F.; Driba, D.L.; Hennings, J.; Kappler, A.; Naumann, R.; Reinsch, T.; Schubert, C. Mineral precipitation during production of geothermal fluid from a Permian Rotliegend reservoir. *Geothermics* **2015**, *54*, 122–135. [[CrossRef](#)]
20. Ma, Z.; Xu, Y.; Zhai, M.; Wu, M. Clogging mechanism in the process of reinjection of used geothermal water: A simulation research on Xianyang No.2 reinjection well in a super-deep and porous geothermal reservoir. *J. Groundw. Sci. Eng.* **2017**, *5*, 311–325.
21. Yanaze, T.; Yoo, S.; Marumo, K.; Ueda, A. Prediction of permeability reduction due to silica scale deposition with a geochemical clogging model at Sumikawa Geothermal Power Plant. *Geothermics* **2019**, *79*, 114–128. [[CrossRef](#)]
22. Zhao, Y.; Feng, B.; Zhang, G.; Shangguan, S.; Qi, X.; Li, X.; Qiao, Y.; Xu, J. Study of the interaction between the granitic hot-dry rock (HDR) and different injection waters. *Acta Geol. Sin.* **2020**, *94*, 2115–2123.
23. Ke, Z.; Feng, B.; Liu, Y.; Cui, Z.; Liu, X. Dissolution and sedimentation patterns of typical minerals in artificial reservoirs under different environment. *Unconv. Resour.* **2022**, *2*, 60–71. [[CrossRef](#)]
24. Feng, C.; Gao, G.; Zhang, S.; Sun, D.; Zhu, S.; Tan, C.; Ma, X. Fault slip potential induced by fluid injection in the Matouying enhanced geothermal system (EGS) field, Tangshan seismic region, North China. *Nat. Hazards Earth Syst. Sci.* **2022**, *22*, 2257–2287. [[CrossRef](#)]
25. Qi, X.; Shangguan, S.; Zhang, G.; Pan, M.; Su, Y.; Tian, L.; Li, X.; Qiao, Y.; Zhang, J. Site selection and developmental prospect of a hot dry rock resource project in the Matouying Uplift, Hebei Province. *Earth Sci. Front.* **2020**, *27*, 94–102.
26. Shangguan, S. Occurrence conditions of hot-dry-rock geothermal resources and development prospects in Matouying area. *China Energy Environ. Prot.* **2017**, *39*, 155–165.
27. Zhang, Y.; Gao, L.; Liu, X.; Zhao, Y.; Wang, D.; Zhang, J. Drilling technology of the M-1 well in hot dry rock of Matouying, Tangshan. *Geol. Explor.* **2022**, *58*, 176–186.
28. Xu, T.F.; Spycher, N.; Sonnenthal, E.; Zhang, G.X.; Zheng, L.E.; Pruess, K. TOUGHREACT Version 2.0: A simulator for subsurface reactive transport under non-isothermal multiphase flow conditions. *Comput. Geosci.* **2011**, *37*, 763–774. [[CrossRef](#)]
29. Xu, T.; Sonnenthal, E.; Spycher, N.; Pruess, K. *TOUGHREACT User's Guide: A Simulation Program for Non-Isothermal Multiphase Reactive Geochemical Transport in Variably Saturated Geologic Media*; V1.2.1; Lawrence Berkeley National Lab. (LBNL): Berkeley, CA, USA, 2008.
30. Xu, T.; Hu, Z.; Feng, B.; Feng, G.; Li, F.; Jiang, Z. Numerical evaluation of building heating potential from a co-axial closed-loop geothermal system using wellbore–reservoir coupling numerical model. *Energy Explor. Exploit.* **2020**, *38*, 733–754. [[CrossRef](#)]
31. Qi, X.; Zhang, G.; Shangguan, S.; Su, Y.; Tian, L.; Li, X.; Qiao, Y.; Liu, X. A brief analysis of hot and dry rock geothermal resource hosting and distribution in Hebei Province. *Coal Geol. China* **2018**, *30*, 47–73.
32. Cui, Z.; Shangguan, S.; Gherardi, F.; Qi, X.; Xu, J.; He, S.; Feng, B. Experimental Study on the Effect and Mechanism of Chemical Stimulation on Deep High-Temperature Granite. *Front. Earth Sci.* **2022**, *10*, 893969. [[CrossRef](#)]
33. Shangguan, S.; Sun, D.; Zhang, G.; Yang, Y.; Qi, X.; Chen, D.; Qiao, Y.; Li, A.; Chen, Q. In-situ stress measurement and fault stability analysis within a depth of 3–4 km in the Tangshan area. *Acta Geol. Sin.* **2021**, *95*, 3915–3925.
34. Xu, J.; Feng, B.; Cui, Z.; Liu, X.; Ke, Z.; Feng, G. Comparative Study of Acid and Alkaline Stimulants with Granite in an Enhanced Geothermal System. *Acta Geol. Sin.* **2021**, *95*, 1926–1939. [[CrossRef](#)]
35. Na, J.; Xu, T.F.; Jiang, Z.J.; Bao, X.H.; Wu, Y.D.; Feng, B. A study on the interaction of mud acid with rock for chemical stimulation in an enhanced geothermal system. *Environ. Earth Sci.* **2016**, *75*, 1025. [[CrossRef](#)]
36. Yang, Z.; Wang, F.; Yang, B.; Tian, H.; Xu, T. Numerical simulation of the influence of Chlorite on the content of mineral trapping of CO<sub>2</sub> in the sandstone. *Bull. Mineral. Petrol. Geochem.* **2014**, *33*, 201–207.
37. Xue, W.; Tan, X.; Li, Z.; Qiu, Y.; Yong, Y.; Jiang, W. Dissolution mechanism of feldspars in the clastic rocks and its contribution to diagenesis. *Complex Hydrocarb. Reserv.* **2015**, *1*, 1–6, 61.